Microscopy and Microanalysis, 2023, **00**, 1–11
https://doi.org/10.1093/micmic/ozac057

Microscopy AND Microanalysis

Original Article

Vanadium Electronic Configuration Determination From $L_{2,3}$ Transition in V-oxide Compounds and Roscoelite

Pierre-Marie Zanetta[1,*], Maxwell S. Drexler[2], Isabel F. Barton,[2] and Thomas J. Zega[1,3]

[1]*Lunar and Planetary Laboratory, The University of Arizona,1629 E University Blvd, Tucson, AZ 85721, USA*
[2]*Mining and Geological Engineering, The University of Arizona, 1235 James E. Rogers Way, Tucson, AZ 85719, USA*
[3]*Materials Science and Engineering, The University of Arizona, 1235 James E. Rogers Way, Tucson, AZ 85719, USA*

*Corresponding author: Pierre-Marie Zanetta, E-mail: pierre.marie.zanetta@gmail.com

Abstract

We report on the electronic structure of vanadium in synthetic V-oxides and in natural roscoelite (V-rich phyllosilicate). This study applied electron energy-loss spectroscopy (EELS) in the scanning transmission electron microscope (STEM), combined with first-principle calculations, to (1) establish relationships between the V oxidation state and EELS $L_{2,3}$ features and (2) better constrain the oxidation state and crystallographic siting of V in roscoelite, with implications for other V-bearing phyllosilicates. Both EELS measurements and band structure calculations show that the EELS L_2/L_3 ratio increases as the oxidation state of V increases. We establish a quantitative relationship between the V $L_{2,3}$ near-edge structure and the V oxidation state by normalizing the L_2 maximum peak intensity to the L_3 peak intensity. By applying this method to roscoelite, we find that it hosts a mix of trivalent and tetravalent V distributed between the octahedral and tetrahedral sites with a $V^{4+}/\Sigma V = 0.6 \pm 0.1$. This relationship is applicable to measurements of V oxidation states in oxide and phyllosilicate minerals, which is useful for constraining the conditions of rock and mineral formation and has potential implications for metal extraction from phyllosilicate ores.

Key words: DFT calculations, STEM-EELS, site occupancy, V oxidation state, vanadium

Introduction

The intrinsic oxidation state of a material is related to the temperature, the composition, and the oxygen fugacity (fO_2) of the system at its origin. Thus, oxidation states of elements in natural samples can provide fundamental information on the chemical and physical conditions under which they formed or last equilibrated (Schreiber et al., 1978; Mysen et al., 1984; Ballhaus et al., 1990; Frost, 1991; Petit et al., 2001; Frost & McCammon, 2008; Tian et al., 2016; Moretti & Neuville, 2021; Roskosz et al., 2022). For example, Berry et al. (2008) use the Fe oxidation state of a komatiitic melt inclusion to investigate the relationship that can exist between the $Fe^{3+}/\Sigma Fe$ and the conditions (temperature, composition, water content, and fO_2) of the silicate melt at their origins.

Several elements may be used to help constrain the redox state of the system. The most commonly used are the 3d metals because they can occur naturally in various oxidation states and are reactive elements (Schreiber et al., 1978; Zega et al., 2003; Simon et al., 2007; Chi et al., 2009; Tan et al., 2011, 2012; Zanetta et al., 2022). One such 3d metal, vanadium (V), is widely distributed in earth and planetary materials. The prevailing valence states of V in nature are V^{3+}, V^{4+}, and V^{5+}; more reduced species containing V^{2+} and V metal are possible but vanishingly rare under earth conditions (Ostrooumov & Taran, 2016). It is common for V-oxides to contain V in mixed valence states, e.g., V_3O_5, V_4O_7, V_6O_{11}, V_6O_{13}.

V is overall lithophile, and most of the numerous (>250) minerals that it forms are hydroxides or complex oxides, e.g., phosphates, vanadates, and silicates. The V-oxides are widely studied because of their material properties. V_2O_3, VO_2, and V_2O_5 are defined as transition metal oxides (TMOs) that can exhibit an abrupt change in their conductivity and transition from metallic to insulator above a critical temperature (T_c) (Lamsal, 2014). They have unique physical, electronic, and magnetic properties and are of potential interest in numerous technologic applications, e.g., cathode material for batteries, temperature sensors, and photo-induction (Lamsal, 2014; Zhou & Ramanathan, 2015). Vanadium trioxide (V_2O_3) is the only phase that naturally occurs above its critical temperature (160 K) and at room temperature is metallic with a trigonal corundum structure and space group $R\bar{3}C$. Vanadium dioxide (VO_2) shows its transition very close to room temperature (340 K) but occurs as a monoclinic (space group $P2_1/c$) crystal structure. Finally, vanadium pentoxide shows the highest transition temperature ($T_c = 530$ K) and occurs at room temperature as orthorhombic lattice with space group Pmmn (No. 59). In comparison, two relatively common V minerals, the oxyhydroxide montroseite (V, Fe)O(OH) and the phyllosilicate roscoelite (a V-bearing mica idealized as $K(V, Al)_2(AlSi_3)O_{10}(OH)_2$) (Brigatti et al., 2003), are commercially mined V ores.

Constraining the crystal chemistry of V in synthetic and natural materials is therefore important but requires techniques that can characterize the crystallographic siting of V as well as its electronic configuration (Loehman et al., 1969; Rakotoniaina et al., 1993; Lamsal, 2014; Marcelli et al., 2017). There are numerous methods for determining element concentrations in materials, but few of these methods can distinguish between different oxidation states or sites. The most common techniques sensitive to oxidation state are spectroscopic: Mossbauer spectroscopy (Mysen et al., 1984;

Received: October 11, 2022. **Revised:** December 17, 2022. **Accepted:** December 26, 2022

Holtstam, 1996; Jayasuriya et al., 2004; Roskosz et al., 2022), X-ray absorption near-edge structure in the scanning transmission X-ray microscope (STXM) (Petit et al., 2001; Simon et al., 2007; Le Guillou et al., 2015), and EELS in the transmission electron microscope (TEM) (Garvie et al., 1994; Garvie & Buseck, 1998; Van Aken et al., 1998; Van Aken & Liebscher, 2002; Zega et al., 2003; Tan et al., 2011, 2012; Bourdelle et al., 2013; Zanetta et al., 2022). However, V does not have an isotope suitable for oxidation state measurements by Mossbauer. Furthermore, because V mainly occurs in complex minerals with multiple sites that can accommodate 3d metals, high-resolution techniques that can resolve the site occupancy are important. STXM is a high spectral resolution (0.1 eV) technique, but is spatially limited to a few tens of a nanometer and so, while it can provide useful information on crystal chemistry, it cannot provide atomic-scale site location of the V. In contrast, new-generation aberration-corrected TEMs can achieve atomic resolution while integrating EELS spectroscopic measurements with enough spectral resolution (<0.4 eV in cold field emission; <0.1 eV if monochromated) to obtain information on electronic structures of *3d* metals in a wide range of materials (Muller et al., 2008; Ek et al., 2017; Zanetta et al., 2022).

The electronic structures and spectroscopic signatures of 3d metals are complex due to their sensitivity to numerous parameters including bonding, electronic neighborhood, mixed oxidation state, crystal-field effects, and thermoelectric transitions like TMOs (e.g., Fischer, 1970; Stoyanov et al., 2007; Lamsal, 2014; Levina et al., 2014; Zanetta et al., 2022). Thus, a combined approach involving experimental EELS and density functional theory (DFT) is a powerful tool for determining oxidation states of 3d metals and the underlying physics of electronic transitions (e.g., Leapman et al., 1982; Brik et al., 2006; Hébert, 2007; Virdi et al., 2013; Lamsal, 2014; Nuñez, 2019; Zanetta et al., 2022). DFT calculations, in the last decade, have become more widely used in studying electronic structures and to confirm spectral features (Hébert et al., 2003; Hébert, 2007; Blaha et al., 2011, 2020). This computational method can provide insight into the crystal chemistry and the effect of site occupancy on the spectral features (Zanetta et al., 2022).

Here, we examine the electronic structure of V in a series of synthetic oxide standards and in roscoelite, a representative silicate mineral that naturally occurs with a high V concentration. The oxidation state of V and its crystal chemistry in roscoelite are determined via EELS in an aberration-corrected STEM. Obtained $L_{2,3}$ spectra are compared with the complementary information obtained by DFT calculations. On the basis of these experimental and modeled results, we report a method for the quantification of the V oxidation state in V-bearing oxides and phyllosilicates using EELS and examine V siting and oxidation state in roscoelite.

Materials and Methods

Samples

We acquired three high-purity (>99.8%) standards with known oxidation states (V_2O_3, VO_2, and V_2O_5) from commercial suppliers (Alfa Aesar and SigmaAldrich) in the powder form. Standards were crushed in an agate mortar and pestle in dry conditions and deposited onto lacey-carbon films supported by Cu-mesh TEM grids (Zanetta et al., 2022). We measured several particles that were monodisperse and electron transparent (<50–60 nm in thickness).

We also examined a roscoelite $K(V, Al, Mg)_2AlSi_3O_{10}(OH)_2$ sample from the Omega mine above Placerville, Colorado (Supplementary Table S1). The roscoelite composition was quantified using a Cameca SX100 electron microprobe located in the University of Arizona's Kuiper Materials Imaging and Characterization Facility (KMICF). A 2-μm probe with an accelerating voltage of 15 kV and beam current of 20 nA was used for analyses. Mg, Na, Si, and Al intensities were acquired on a TAP crystal; Ca, Ti, K, Cr, V, P, Sr, and Cl on an LPET crystal; and Fe, Mn, Cu, and Co. on an LLIF crystal. Standards for the microprobe measurements are given in the Supplementary Material.

We prepared electron-transparent cross sections of the roscoelite sample using the ThermoScientific (formerly FEI) Helios NanoLab 660 G^3 focused ion beam (FIB) scanning-electron microscope also located in KMICF. The general procedures of FIB sample preparation, e.g., coarse cutting, lift out, and *in situ* thinning, have been previously described (Zega et al., 2007, 2020; Zanetta et al., 2022).

STEM

The V standards and the roscoelite sample were measured using a 200 keV aberration-corrected Hitachi HF5000 scanning TEM (S/TEM). The HF5000 is equipped with a cold field-emission gun, a third-order spherical-aberration corrector for STEM mode, bright-field and annular dark field STEM detectors, and a Gatan Quantum ER (model 965) electron energy-loss spectrometer (EELS). EELS spectra were acquired using a 200 keV acceleration voltage, a 10 μA emission current, and 3.45 eV extraction voltage, a STEM condenser aperture of 35 μm, and a 2 μs dwell time. All EELS spectra were corrected for channel-to-channel gain variation and dark current. We used a probe current of 330 pA and a collection angle of $\beta = 63$ mrad. We used a 2.5 mm EELS entrance aperture and a dispersion of 0.25 eV/channel corresponding to a 1.0 eV zero-loss peak full-width half-maximum (ZLP FWHM). Both low-loss and core-loss spectra were acquired simultaneously ("dual EELS mode"), and a pixel time of 0.2 s for the core loss was used and 0.001 s for the low loss. Phyllosilicates can be sensitive to the electron beam, and so we optimized our electron-optical conditions to minimize beam damage. Thus, we acquired spectrum images of 15 × 10 pixels and ultimately summed the pixels to increase the signal-to-noise ratio. Hence, we used a large collection angle and short integration time to, respectively, minimize the local electron dose and decrease the exposure time. We fixed a pixel size of 1.5 nm for synthetic oxides and 15 nm for roscoelite.

Spectra were processed using personal Python scripts (Zanetta et al., 2022 and available at: https://github.com/ZanettaPM/Ti-Oxidation-EELS-data-processing) constructed using Hyperspy (de la Peña et al., 2022). The energy positions of the low-loss and high-loss spectra from different pixels were calibrated via zero-loss peak (ZLP) centering. The π^* peak of the C K edge at 285 eV, acquired with the same energy dispersion, served as a calibration point. An inverse power law (AE^{-r}) model, where E is the energy loss and A and r are constants, was used to subtract the background. An energy window measuring 50 eV, placed between 450 and 500 eV (for a 0.25 eV/channel dispersion), was used to fit the background

function. The plural scattering contributions due to sample thickness were removed by Fourier-ratio deconvolution.

Density Functional Theory

We used the DFT to simulate spectra and constrain the electronic configuration of the standards and the roscoelite. We computed the electronic band structure of the V standards and roscoelite by means of the linearized augmented plane wave method, as implemented in the Wien2k package (Blaha et al., 2020), and approximations to the exchange-correlation by generalized gradient approach functionals (Perdew et al., 1996). Electronic structure calculations were conducted starting with experimentally reported crystal structures (Tables 1a and 1b, Supplementary Table S2). Initialization parameters and self-consistent field (SCF) calculation convergence rules were set according to Hébert (2007). The energy to separate core and valence states was fixed at −6 Rydberg (Ry; 1 Ry ≈ 13.605 eV), except for the sample containing Al where a value of −8 Ry was adopted because of its atomic configuration. This separation in energy enables the simulation of a mixture of 3 s, 3p, 3d, and 4 s V orbitals with 2 s and 2p O orbitals in our density-of-state calculations for V-oxides. The matrix size RKmax ($R_{mt} * K_{max}$) was kept fixed at 7.0, where K_{max} is the plane wave cutoff and R_{mt} is the smallest atomic sphere. Convergence criteria for the SCF cycle were fixed at 0.00001 Ry and 0.5 mRy/au for the energy and the force, respectively. After optimization of the structure, we proceeded to the next iteration with higher k-mesh points (sampling points in the irreducible wedge of the first Brillouin zone of the material) until the theoretical electron energy-loss near-edge spectra (TELNES) between two iterations became nearly identical (average difference of the intensity integrated over the energy range being <5%). For simulating the roscoelite spectra, we attempted to relax three distinct crystal structures. One calculation is a natural roscoelite with a complex crystal chemistry that breaks the symmetry of the space group (C2/m) but accounts for the various V crystallographic siting and all possible atomic neighbors $K(V^{3+}, V^{4+})_2(AlSi_3)O_{10}$, whereas two others are poly types with the same structures but simplified compositions, Roscoelite(3+): $Ba(V^{3+})_2(Al_4)O_{10}$ and Roscoelite(1:3): $K(Mg)_2(V^{3+}{}_1V^{4+}{}_3)O_{10}$ ($V^{3+}/V^{4+} = 0.33$). The two latter crystal chemistries conserve the space group symmetry and simulate two distinct V site configurations, octahedral and tetrahedral, respectively. We established these endmember compositions to satisfy (1) the electro-neutrality of the structure (without the presence of the OH radicals), (2) the atomic neighbors as expected in the solid solution (K, Ba, Mg, Al, Si, and O), and (3) the expected oxidation state of the V according to the site coordination (i.e., the V is expected to be V^{3+} on the octahedral site and mostly V^{4+} on the tetrahedral site; Brigatti et al., 2003). Although these simulations are not exact replicas of the natural samples, they correctly simulate the electronic environment of the V in roscoelite while allowing the correct relaxation of the structure.

The TELNES3 program implemented in Wien2k was used to model EELS spectra from density-of-state calculations (Jorissen, 2007). The splitting energy and the branching ratio were calculated statistically. We assumed no orientation dependence, and so we averaged our calculations over all possible directions of the scattering vector with respect to the crystal. Spectral broadening was always simulated with the same conditions, i.e., no linearly energy-dependent valence broadening and a Gaussian spectrometer broadening set at 0.8 and 2.3 eV. The former broadening value was used to investigate peak splitting for lower experimental energy dispersions (<0.25 eV/channel) in EELS. The latter broadening value does not correspond to our experimental ZLP full-width-half-maximum (FWHM) but acts as a correction factor to obtain similar V $L_{2,3}$ peak widths as the experimental spectra. We fixed a factor of 2 on the second spectrum contribution in our broadening setup to match the experimental L_2/L_3 peak ratio. We kept the core-hole lifetime of the two edges as tabulated in the TELNES3 program.

Results

We acquired EELS spectra at the V $L_{2,3}$ edge for V-oxide standards and roscoelite to examine their electronic structure, compare it to our DFT calculations (Table 1), and investigate a relationship between oxidation states and spectral features. The representation of the V-compound crystal structures is given in Figure 1. Figure 2a shows the experimental spectra normalized to the individual maxima of the first peak (V_{L3}, energy range: 514.0–521 eV) acquired from the V-bearing reference materials. The normalization suppresses the variations in absolute intensity and the effects of thickness or concentration. Experimental spectra (Fig. 2a) show the two L_3 and L_2 peaks at approximately 518 and 525 eV (labeled a and b, see Supplementary Table S3). The synthetic oxide spectra show a clear chemical shift at the V $L_{2,3}$ edge that correlates with the valence state of the material. The energy positions of the peaks (Supplementary Table S3) are in agreement with previous measurements of V $L_{2,3}$ spectra of V-oxides (Fischer, 1970; Brik et al., 2006; Tan et al., 2012; Levina et al., 2014). As the V oxidation state increases, the intensities of peaks "b" and "c" increase in comparison to peak "a". Peak "c" corresponds to the pre-edge peak of the O-K edge. In comparison, the roscoelite sample shows a significantly more intense O peak and an onset energy value superior to VO_2 (512.8 versus 512.5 eV).

We also computed EELS spectra for the V-oxide standards and roscoelite. Figure 2b shows the simulated spectra with minimum broadening. In our simulation, the "natural" roscoelite calculation did not converge within the computational resources due to the complexity of its structure, but all other calculations converged successfully (Fig. 2b). Features that compose the L_3 and L_2 edges are visible (Supplementary Fig. S1). The two edges are composed of three peaks (a, a′, and a″, and b, b′, and b″). We hereafter discuss samples in order of increasing oxidation (i.e., V_2O_3, Roscoelite (3+), Roscoelite (1:3), VO_2, V_2O_5). Samples with the lower oxidation state (the 3+ blue and pink lines Fig. 2b) show a higher subpeak than a′ and not a″. As the oxidation state increases, the peaks a″ and b″ increase in intensity. In VO_2 and Roscoelite (1:3), subpeaks a′, and b′ increase and reach about the same intensity as the a and b peaks. The subpeaks a″ and b″ increase significantly. In V_2O_5, peaks a and b decrease compared to VO_2, whereas the intensities of peaks a″ and b″ keep increasing. We note that peaks c and c″ display no consistent trend with the increasing oxidation state because they reside on top of the O-K edge, and only the V $L_{2,3}$ line is modeled in our calculations.

Figure 3 compares the experimental with no broadening (see Supplementary Fig. S2) and simulated spectra after

Table 1. Calculation Setup Parameters for the SCF Calculation of the Different Species.

Standard	Oxidation State	Space Group	Tc for IMT	RMT V a.u.	RMT O a.u.	RKMax ($R_{mt} * K_{max}$)	Energy Threshold (Ry)	Final K-mesh Points	Initial cif File
V_2O_3	3+	R-3C	160 K	1.84	1.66	7	−6	100	Newnham and Haan, 1962
VO_2	4+	$P2_1/c$	340 K	1.61	1.46	7	−6	100	Rakotoniaina et al., 1993
V_2O_5	5+	Pmmn	530 K	1.56	1.41	7	−6	100	Ketelaar, 1936
Roscoelite (3+)	3+	C2/m	Nd	1.97	1.53	7	−8	100	Brigatti et al., 2003
Roscoelite (1:3)	3.75+	C2/m	Nd	1.61	1.46	7	−6	100	Brigatti et al., 2003

Space Group Shown in Hermann–Mauguin Notation.
IMT, insulator to metal transition; RMT, muffin-tin radius. The sampling points in the Brillouin zone are given as K-mesh. Visualization of the structures is presented in Figure 1.

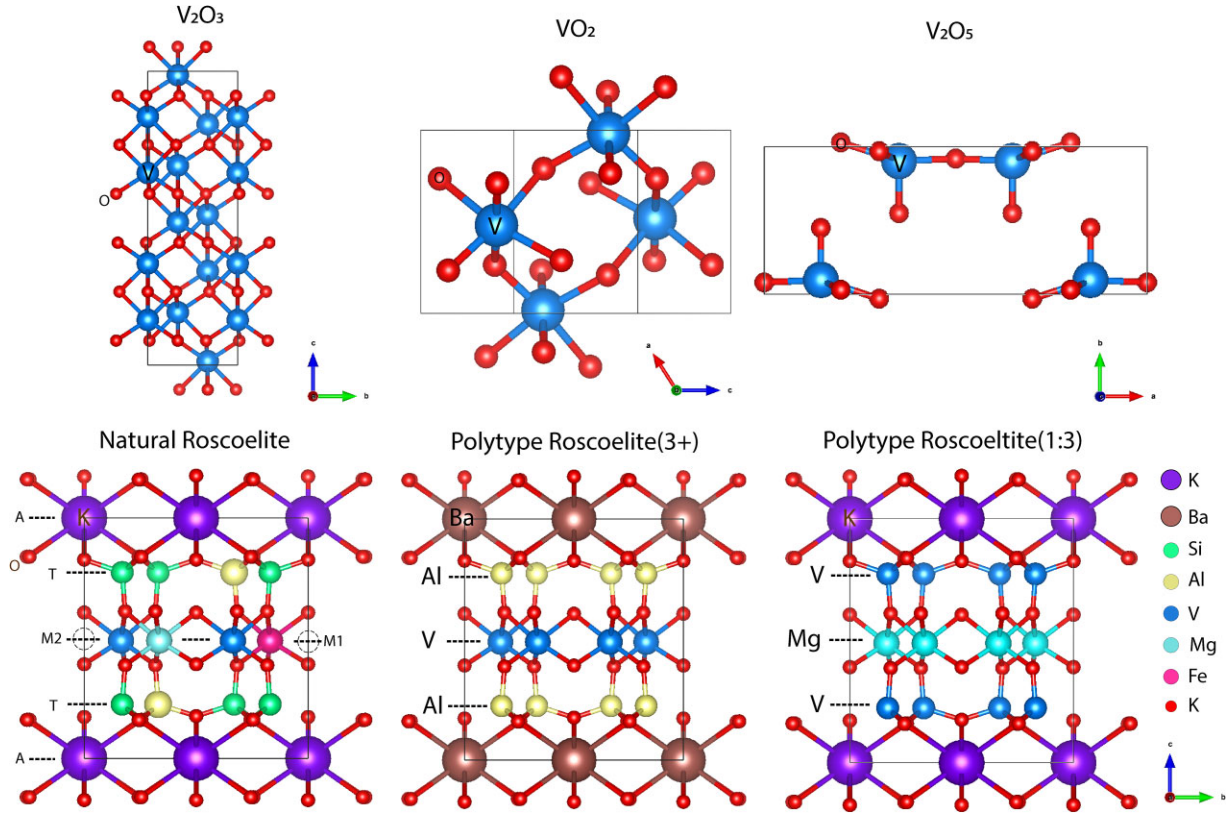

Fig. 1. Ball-and-stick representation of the v-compound structures. The structures are presented along the best orientations (a, b or c) to facilitate the visualization of the geometries. Two "idealized" polytypes of the roscoelite crystal are presented Roscoelite(3+) and Roscoelite(1:3). They represent a simplified version of the crystal chemistry with respect to the space group symmetry. Each color represents one atom. The color code is indicated in the bottom right corner.

broadening to account for experimental dispersion. The computed spectra reproduce the peaks and positions in the experimental spectra of V-oxides collected using EELS. After normalization to the L_3 intensity, the L_2 intensity increases with the increasing oxidation state (Figs. 3a and 3b, dashed lines and dark arrows). Figure 3b shows that the L_3 and L_2 peaks of the roscoelite experimental spectrum plot at similar energies to that of the R(1:3) calculated spectrum (517.7 and 524.5 eV, respectively) and at higher energies than R(3+) (515.8 and 523.0 eV), respectively, Supplementary Table S3). The simulated V L_2 and L_3 peak widths are smaller for the roscoelite R(3+) compared to V_2O_3 despite having the same oxidation state.

The onset energy of the V edge in roscoelite (512.8 eV) occurs at a higher energy than tetravalent V (512.5 eV) as represented by VO_2. Therefore, the use of the identified chemical shift, by itself, for the quantification of the V oxidation state in roscoelite is problematic because stoichiometry suggests V^{3+} to V^{4+} for charge balance. So, we explored an alternative approach to quantify the V oxidation state in roscoelite. Our TELNES calculations show that the increase of the b peak (L_2) is predominantly dependent on the oxidation state regardless of specific site occupancies and those effects on the ELNES (Fig. 3, dark arrows, and Fig. 4). Thus, the L_2 maximum intensity (after normalization) depends on the V oxidation state and can be used for quantifying it. We find that the maximum

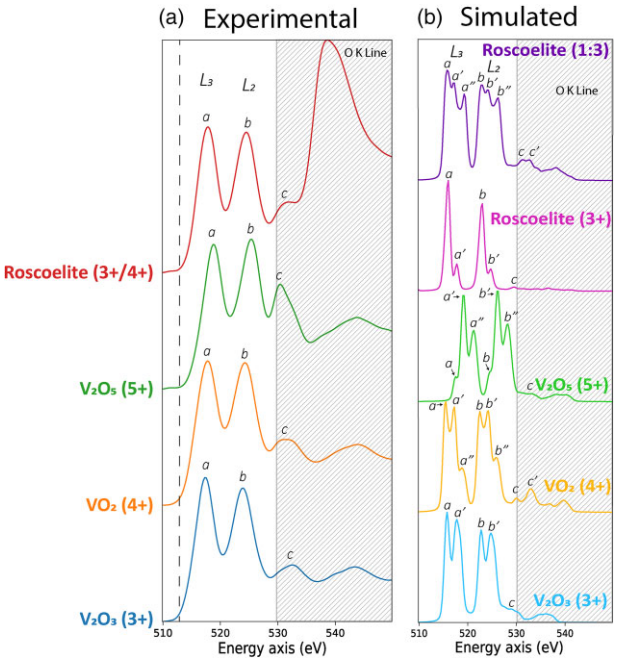

Fig. 2. Experimental and simulated $VL_{2,3}$ spectra normalized to the maximum intensity of the L_3 peak. The O-K line contribution is not included in the simulation. (**a**) Experimental spectra of the V-oxides and the Placerville roscoelite. The O-K line is shadowed (530 to 550 eV panel). (**b**) Simulated spectra from Wien2K with limited (0.8 eV) broadening, allowing a more complete description of the spectral features.

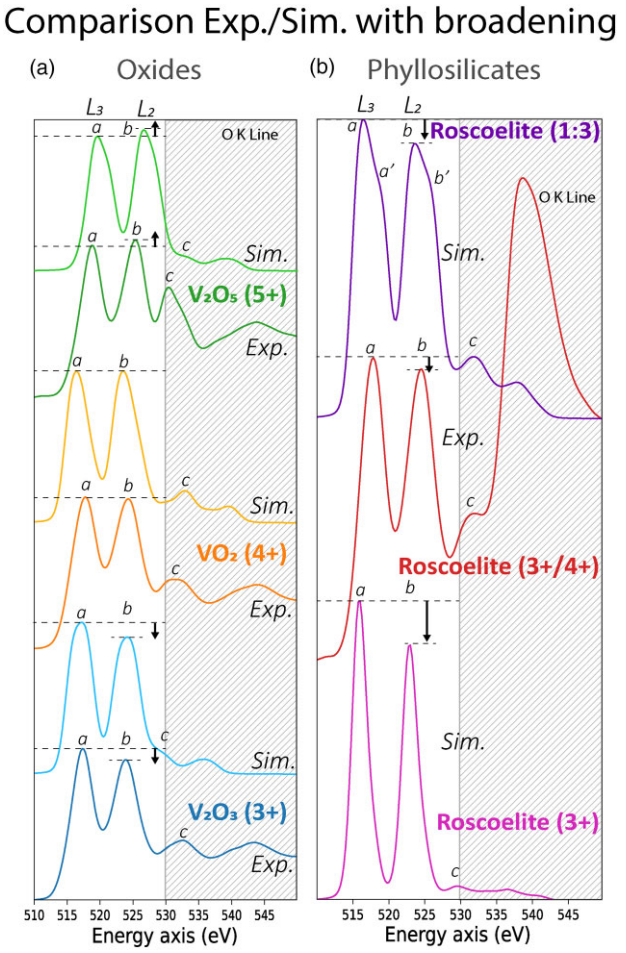

Fig. 3. Experimental and simulated $VL_{2,3}$ spectra normalized to the maximum intensity of the L_3 peak. The O-K line contribution is not included in the simulation. (**a**) Comparison of the simulated and experimental spectra for the V-oxides only (same color family represent the same structure). The simulated spectra from Wien2K are broadened (2.3 eV) to match the $L_{2,3}$ peak width of the experimental spectra. The black arrows highlight the increase of the L_2 intensity in comparison of the L_3 peak (dashed line) as function of the oxidation state, which is reproduced by the simulations. (**b**) Comparison of the experimental and simulated roscoelite materials. The O-K line is shadowed.

intensity of the L_2 peak increases as a function of the increasing oxidation state (Fig. 4). A best fit to the experimental data on the oxides gives:

$$y = 0.054x + 0.768 \quad (1)$$

with $R^2 = 0.99$ (Fig. 4).

The fitted line defined by equation (1) is compared to the fitted line defined by the simulated spectra (dashed blue line in Fig. 4 with $y = 0.088x + 0.613$ and $R^2 = 0.86$). On the basis of scattering of the experimental data points from the oxide standards around the fitted line, we estimate an absolute error of ~10% for the determination of the V oxidation state (dashed black lines, Fig. 4) by this method. The application of this method to the roscoelite sample (R in Fig. 4) yields a $V^{4+}/\Sigma V$ ratio of 0.6 ± 0.1 corresponding to a V^{3+}/V^{4+} ratio of 0.4 (see Fig. 3 for comparison with simulated polytypes).

Discussion

Electronic Structures of V-Oxides

The V-oxides and roscoelite samples analyzed in this study show different structures and crystal chemistries (Table 1 and Fig. 1). The neighborhood of V and its interaction with O in each of these structures generates distinct ELNES spectral features (Figs. 2 and 3). The interaction between the V 3d orbital and O 2p orbital forms the $2e_g$ and $1t_{2g}$ bonding and $2t_{2g}$ and $3e_g$ antibonding molecular orbital levels described in Figure 5 (Fischer, 1970; Stoyanov et al., 2007; Zanetta et al., 2022). Electronic transitions from the core level to empty states above the Fermi energy (E_f) are responsible for EELS edges (Fig. 5). For 3d metals like V, the L_3 and L_2 peaks originate from electronic transitions of the $2p^{3/2}$ and $2p^{1/2}$ core levels, respectively, to 3d levels (i.e., the antibonding orbitals $2t_{2g}$ and $3e_g$). Such combinations sometimes lead to the generation of four distinct peaks due to the splitting of the five degenerate states into the twofold $3e_g$ and the threefold $2t_{2g}$ level, as is the case in Ti $L_{2,3}$ (Stoyanov et al., 2007). However, the splitting energy (<1.5–2 eV) of the $3e_g$ and $2t_{2g}$ levels in V is too small to be resolved with the present energy resolution in the EELS spectra due to spectral broadening. Although the ZLP resolution is 1 eV (FWHM), EELS spectral broadening varies with the energy loss because both the spectrometer focusing and the angular width of inelastic scattering are energy dependent. As a result, the energy resolution at an ionization edge can be worse than that measured at the ZLP (Egerton, 2011). Nonetheless, these levels are easily visible in our simulations, e.g., peaks a and a′ and b and b′ in the V_2O_3 spectrum, which are shown with a smaller broadening energy (Fig. 2b). The splitting energy and the intensity of the peaks depend on various factors as well as the oxidation state, including the site symmetry and the crystal field (Fischer, 1970; Leapman et al., 1982; Stoyanov et al., 2007).

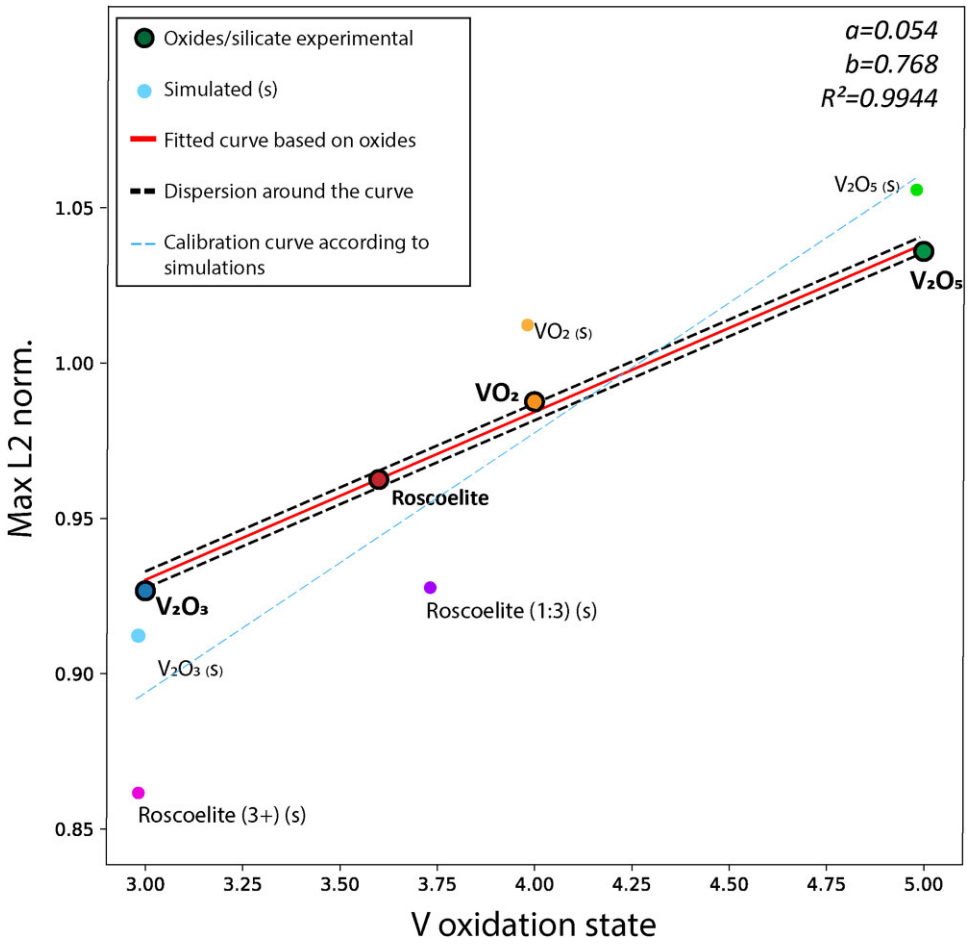

Fig. 4. Fitted relationship between the maximum L_2 peak height after normalization and the vanadium oxidation state as measured and computed for the oxide standards. Both results from the experimental and simulated spectra are represented. Only the experimental oxide data are used to fit the calibration curve. The theoretical curve fitted based on the simulated spectra is represented (blue dashed line).

The energy of the two orbital levels (i.e., the $3e_g$ and $2t_{2g}$) can be exchanged (one passing above the other in terms of energy, Fig. 5) depending on whether the V occupies a tetrahedral or octahedral site (Zhou & Ramanathan, 2015). However, it was shown that the $3e_g$ and the $2t_{2g}$ levels exhibit close energy states for V (Lamsal, 2014). These results suggest that the configurational mixing of the $3e_g$ and $2t_{2g}$ levels and octahedral distortions cannot be measured with the energy dispersion used in this study. We conclude that the effects of the degenerate states on the spectral features (Fig. 2b) are convoluted in the broadened L_2 and L_3 peak intensities (Fig. 3) but do not impact our established relationship between the V oxidation state and EELS $L_{2,3}$ features.

Previous Methods to Quantify V Oxidation State

The results of this study also shed light on the suitability of different methods for analyzing 3d metal oxidation states from EELS spectra of silicates and oxides. The peaks that constitute the V $L_{2,3}$ edge correspond to quantized electronic transitions. Establishing an accurate description of the 3d band structure is useful to understand the connection between the oxidation state and electronic structure (Fig. 5). Among those methods, white-line (WL) ratios have been widely used in the last decades to trace the chemical shift and quantify the oxidation state, and numerous studies in the literature established such a relationship for various 3d metals including Fe, Ti, V, Mn, Cr, Cu, and Ce, e.g., Van Aken et al., 1998; Xu & Wang, 1999; Petit et al., 2001; Van Aken & Liebscher, 2002; Stoyanov et al., 2007; Bourdelle et al., 2013; Kalavathi et al., 2014. Most of these relationships are based on the chemical shift of the edge, i.e., they quantify how the shift in edge energy increases as the oxidation state increases. This shift is mainly due to the increasing of the band gap width and the electron screening efficiency with the oxidation state (Egerton, 2011; Stoyanov et al., 2007; Zanetta et al., 2022).

The WL approach offers an attractive means of tracking the shift in energy in oxide compounds as a function of oxidation state because the effects of the crystal field and coordination environments can be neglected. However, as previously reported by Tan et al. (2012), the WL ratio method is not applicable for V-oxides due to its $L_{2,3}$ edge overlapping with the O-K edge. The application of the WL ratio method developed by Kalavathi et al. (2014) on V-oxides would result in a bulk oxidation state above V^{4+} for roscoelite, which is inconsistent with the expected V^{3+}-to-V^{4+} ratio based on the roscoelite stoichiometry. Indeed, roscoelite exhibits higher edge onset energy than the VO_2 sample and an intense O-K edge, which has the effect of decreasing the counts in the L_3 window but increasing those in the L_2 window. This energy shift yields a

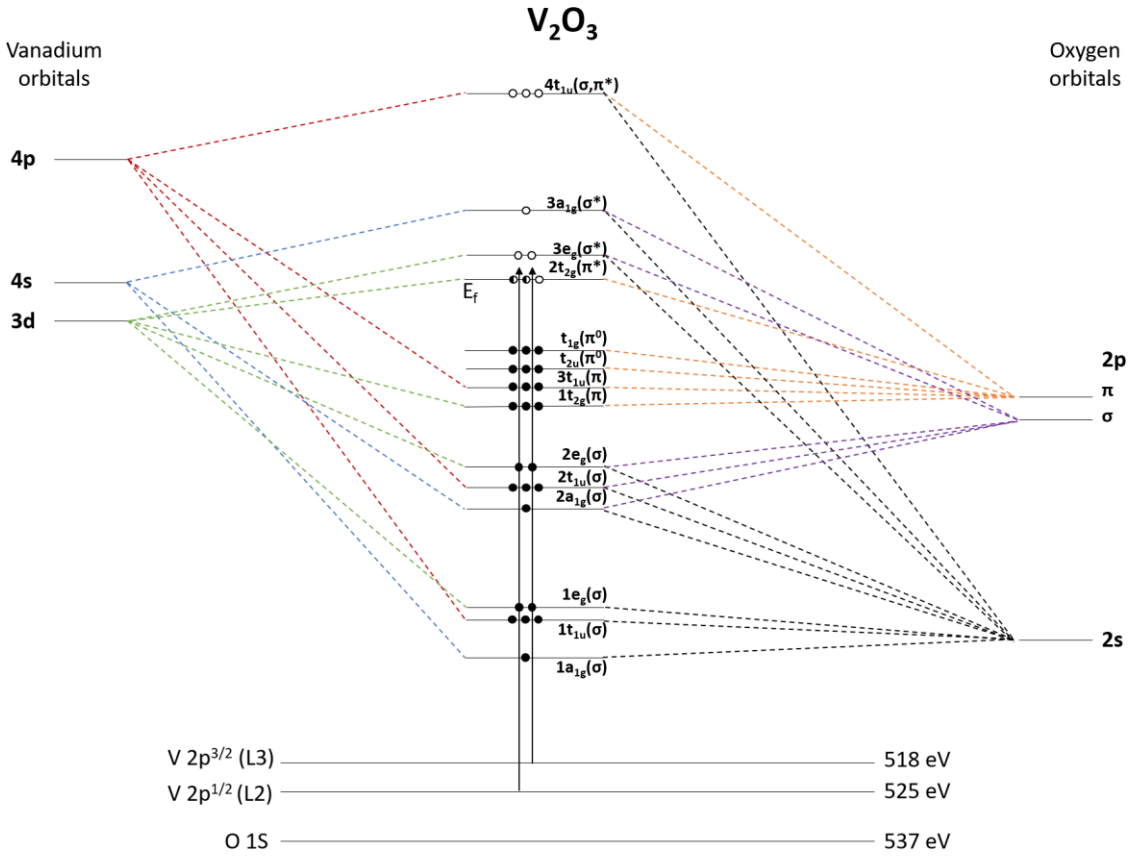

Fig. 5. Molecular orbital diagram for V_2O_3 with two electrons on the $2t_{2g}$ level (half-solid circles). Modified after Fischer (1970). The core state leading to the L_2 and L_3 peak is represented. The transition from the O 1S and the empty state level would correspond to the O-K edge (shadowed region of Fig. 2).

higher L_2/L_3 ratio than VO_2, leading to an overestimation of the V oxidation state in roscoelite.

Another explanation for the nonapplicability of the WL method could be *in situ* sample damage during analysis, causing oxidation and shifting of the edge to higher energy. For example, such damage was observed for the oxidation state of Fe in sheet silicates (Garvie et al., 2004). However, we did not observe any features that suggest beam damage of the V-oxide samples after the EELS acquisition, e.g., shape changes or amorphization. In addition, we used a large field of view (50 × 50 nm) for our measurements to reduce the electron dose and minimize any potential damage of the roscoelite.

Instead of using WL integration windows, other studies used the edge onset energy to quantify the chemical shift of the edge in 3d metals (Tan et al., 2012; Zanetta et al., 2022). However, the application of the edge onset method developed by Tan et al. (2012) to our V compounds would also result in an inconsistent oxidation state for roscoelite (>4+) because the roscoelite spectrum exhibits a higher edge onset energy than the VO_2 sample. We conclude that decoupling the portion of the chemical shift due to the oxidation state versus the electronic environment in roscoelite requires an alternative approach.

One such potential approach is to use the O-K edge to quantify the oxidation state (Stoyanov et al., 2007; Tan et al., 2012). However, the O-K edge can exhibit complex ELNES structures, making accurate simulation difficult (Stoyanov et al., 2007). In this study, a major limitation for the development of a method based on the O-K edge is that the roscoelite spectrum shows an O-K edge significantly more intense than the O-K edge of the V-oxide standards. Further, there are no clear trends in the oxide spectra, e.g., the VO_2 spectrum has a lower O-K edge pre-peak (peak c in Fig. 3) than V_2O_3, but the V_2O_5 spectrum shows a higher O-K peak than V_2O_3. An alternative method developed by Li et al. (2009) used the difference in energy between the L_2 peak and the O pre-edge peak to quantify the V oxidation state. However, the application of this method to our data also resulted in inconsistent V oxidation states for the roscoelite (>5+) because of its intense O-K edge.

Calibration Curve

Other EELS methods use features of the near-edge structure, originating from the electronic configuration for quantifying the oxidation state (e.g., Tan et al., 2012; Bourdelle et al., 2013; Giannini, 2014; Le Guillou et al., 2015; Berry et al., 2017). Here, the combination of experimental and first principle descriptions of the V $L_{2,3}$ edge allows us to define another relationship between the L_2 peak intensity and the V oxidation state while decoupling the effect of the crystal chemistry. The method described here, based on the L_3-normalized intensity of the L_2 peak, uses the occupancy of levels in the V-O molecular orbitals.

In all of the V compounds measured here, the molecular orbitals are filled up to the $t_{1g}(\pi^0)$. When the $2t_{2g}$ is level is almost entirely filled with electrons (as it in the case in V_2O_3), the most probable transition will arise from $2p^{3/2}$ (smaller energy gap, Fig. 5 dark arrows). In this case, the L_3 intensity would be higher compared to the L_2 peak. In the opposite case, if the

$2t_{2g}$ is empty (V_2O_5), then higher-energy transitions from the $2p^{f/2}$ (longer dark arrow) become more probable to fill the $2t_{2g}$ and $3e_g$ levels, and the intensity of the L_2 increases relative to the L_3 peak (energy at which spectra are normalized). Those transition probabilities are used to establish the relationship between the L_2 peak and oxidation state [Eq. (1), Fig. 4]. However, quantifying peak intensities with a simple integration window would lead to inaccurate results due to the chemical shift of the overall edge. To avoid the effects of the shift, we instead used the maximum energy of the peak (in the energy range of 522–527 eV), after normalization to the L_3 peak rather than applying an integration window. The advantage of taking the maximum intensity value is that the channel position where this maximum intensity occurs can vary from one sample to another. This approach led to the relationship shown in Figure 4, based on the L_2/L_3 intensity ratio and which is consistent with the previous work (e.g., Fischer, 1970; Sparrow et al., 1984; Cressey et al., 1993; Kurmaev et al., 2005; Tan et al., 2012; Kalavathi et al., 2014).

The relatively small slope [Fig. 4 and equation (1)] identified in the relationship between the V oxidation state and L_2 intensity is due to normalizing of the L_3 maximum intensity. We note that the difference between the maximum peak intensities in the V-oxide standards L_2 before normalization is generally several thousand counts depending on the integration time, but because the intensities are normalized to 1, the number of counts would not strongly affect the results of the oxidation state calculation. Instead, we quantified the uncertainties based on the dispersion around the fitted curve and the fit residuals. We determine an absolute error of ±10% on the measurements of the oxidation state using this relationship.

We emphasize that the method we report here works accurately within this material system. Other studies show the complexities in applying methods based on ELNES features to materials with electronic structures that are different from the original set of standards on which the method was initially based (Garvie & Buseck, 1998; Zega et al., 2003; Garvie et al., 2004; Tan et al., 2012; Bourdelle et al., 2013; Le Guillou et al., 2015; Zanetta et al., 2022). As noted by Tan et al. (2012), no method exists that can unambiguously and universally determine oxidation states from EELS for all compounds. For instance, numerous papers report height evolution of L_2 and L_3 peaks similar to that presented in this work for pure vanadium oxides (i.e., V_2O_3, VO_2, V_2O_5, e.g., Su & Schlögl, 2002; Gallasch et al., 2011; Kalavathi et al., 2014; D'Elia et al., 2020). However, the previous work also shows a clear reduction of the L_2/L_3 ratio for V^{5+} with the height of L_2 peak lower than L_3 (opposite of what we observe in Fig. 3) for vanadium compounds containing La or Co, i.e., $LaV^{5+}O_4$ and CoV_2O_8 (Fitting Kourkoutis et al., 2006; Tan et al., 2012). The presence of La and Co cations in those V compounds affects their electronic configuration and modify the V L_2/L_3 ratio compared to that of pure V^{5+} oxide studied here (Figs. 3 and 5). Thus, the application of the calibration we report to such a material system would be problematic, highlighting the challenges with developing universal calibration curves.

Evolution of the L_2/L_3 Intensity Ratio

The L_2/L_3 intensity ratio of the 3d metals can be affected by several variables. The previous work suggested that an increase in the L_2/L_3 branching ratio occurs as a function of the oxidation state (Fischer, 1970; Leapman et al., 1982; Sparrow et al., 1984; Cressey et al., 1993; Van Aken et al., 1998; Kurmaev et al., 2005; Brik et al., 2006; Tan et al., 2012; Kalavathi et al., 2014). Sparrow et al. (1984) established that this relationship exists as the d level is filled until $d = 5$. However, Leapman et al. (1982) compared the L_2/L_3 ratio between pure metal and oxide and found that the L_2/L_3 ratio decreases as the oxidation state increases.

We discuss three major difficulties that can lead to confusion about the evolution of the L_2/L_3 ratio as a function of the oxidation state. (1) The common use of integration windows to quantify oxidation states can reinforce the idea that the L_2/L_3 ratio increases with the oxidation state (Van Aken et al., 1998). However, because the position of the windows captures the shift in energy of these transitions, it does not give the exact evolution of the peak intensities and therefore of the L_2/L_3 ratio. (2) The L_2 edge in higher oxidation states exhibits broader spectral features than the L_3 because of the Coster–Kronig Auger decay process, and the use of a static integration window fails to capture this larger energy range and the real L_2/L_3 ratio (Fischer, 1970; Leapman et al., 1982). (3) The removal of the continuum beneath the edge potentially alters the effective L_2/L_3 ratio. Models to remove this continuum have included both straight lines (Garvie & Buseck, 1998; Zega et al., 2003) and step functions (Van Aken et al., 1998; Van Aken & Liebscher, 2002; Stoyanov et al., 2007; Giannini, 2014; Zanetta et al., 2022). Such models have been generally empirical and fit without consideration of an evolving branching ratio (Egerton, 2011; Van Aken et al., 1998; Van Aken & Liebscher, 2002; Stoyanov et al., 2007). Therefore, if the branching ratio is not accounted for, misleading results can arise on the L_2/L_3 ratio.

Here, we did not use fixed windows for integrating the L_2/L_3 ratio. Also, because the V $L_{2,3}$ edge is not strongly affected by the Coster–Kronig Auger decay process, it exhibits well-defined and relatively narrow L_2 peaks (in comparison to the Fe L_2 peak) easing the measurement of its L_2/L_3 ratio. Third, because it is difficult to deconvolve the O-K extended energy-loss fine structure from the V edge, we did not remove the continuum beneath the V edge. This approach potentially limits the artifacts on the L_2/L_3 ratio, because no empirical model is applied to remove the continuum, but requires samples that are sufficiently thin (<50 to 60 nm; Supplementary Table S4). Thus, multiple-scattering contributions should be minimal, and the Fourier-ratio deconvolution that we applied to our data should be sufficient to remove most of the effects due to the thickness variation that could affect the L_2/L_3 ratio. Furthermore, we reproduced our experimental V L_2/L_3 ratio with DFT calculations, independent of the sample thickness, which confirms the relationship established in equation (1) and suggests that it can be used to quantify the oxidation state of phyllosilicates with the structure and the chemistry that are similar to roscoelite (Fischer, 1970; Sparrow et al., 1984; Cressey et al., 1993; Kurmaev et al., 2005; Tan et al., 2012; Kalavathi et al., 2014).

Roscoelite V Oxidation State and Site Occupancy

The oxidation state of V in oxide and silicate minerals is commonly used in numerous earth and planetary science applications. These range from indicators of the chemical conditions of planet formation and evolution to explanations for the inconsistent dissolution behavior of V ores in leaching

(Ballhaus et al., 1990; Canil, 1997; Righter et al., 2006, 2016; Prytulak et al., 2013; Nicklas et al., 2016; Zheng et al., 2019, 2022; Drexler, 2022). The new method presented here offers a reliable, consistent means of measuring V oxidation state in oxides and silicates for these purposes. Previous work on the V oxidation state in roscoelite generally assumes that it substitutes into the crystal structure primarily as V^{3+} in the octahedral layer (Fig. 1) (Foster, 1959; Garrels & Larsen, 1959; Meunier, 1994; Radwany, 2021). However, Wanty & Goldhaber (1985) developed a colorimetric method to measure the V oxidation state in phyllosilicates and compared their results with the thermogravimetric analysis (TGA). Their colorimetric method reported a ratio of $V^{4+}/\Sigma V = 0.15$ in the roscoelite, but TGA gave a result of $V^{4+}/\Sigma V = 0.5$. The latter value is close to our results of $V^{4+}/\Sigma V = 0.6 \pm 0.1$. In addition, our DFT simulations (Fig. 2b) show the increase of the b′ peak and the appearance of a b″ subpeak for increasing oxidation states. These two peaks have the effect of widening the total peak once the broadening is considered. The fact that the a and b peaks in the experimental roscoelite spectrum are larger than those in the simulated Roscoelite (3+) spectrum supports the interpretation that roscoelite contains a mixture of trivalent and tetravalent V. Taken together, these two sets of results strongly suggest that phyllosilicates host a mix of trivalent, probably octahedral, and tetravalent, probably tetrahedral V. This result indicates that the assumption that all phyllosilicate-hosted V is trivalent and octahedral is an oversimplification (Zheng et al., 2019, 2022). Such results could explain the observed variability in V dissolution behavior from phyllosilicate minerals and have implications for V ore extraction (Radwany, 2021; Drexler, 2022; Radwany & Barton, 2022).

Direct observation by STEM-EELS of the position of the V^{3+} and V^{4+} atoms in the atomic lattice would help to confirm our results and provide insights into the crystal chemistry of V-rich phyllosilicate. However, phyllosilicates can be sensitive to the electron beam and amorphize very quickly (Egerton et al., 2004; Garvie et al., 2004; Mignaioli et al., 2009; Egerton, 2013; Ilett et al., 2020). The low vanadium content in roscoelite also requires long EELS acquisition times for detection of its oxidation state. The use of new-generation direct-electron cameras could overcome this problem by increasing the electron detection rate at this energy (Ilett et al., 2020). The development of compressed sensing methods could also allow a decrease in the electron dose and provide enough spatial resolution by using reconstruction algorithms (Li et al., 2018; Stevens, 2018; Taillon, 2018). In addition, the use of cryo-ultramicrotomy and a cryogenic holder could aid in the minimization of beam damage (Jacquemot et al., 2019).

Conclusions

We investigated the electronic structure of V-oxides and roscoelite by STEM-EELS and compared our experimental data with first principles DFT calculations. The results show that the maximum peak intensity of the L_2 edge increases compared to that of the L_3 edge with an increase in the oxidation state. The L_2 edge intensity, normalized to the L_3 edge intensity, is a reliable proxy for the V oxidation state in both oxides and roscoelite, a phyllosilicate V ore. Our data suggest that roscoelite hosts a mix of trivalent and tetravalent V with a ratio of $V^{4+}/\Sigma V = 0.6 \pm 0.1$. Direct atomic-scale measurement of V and its oxidation state in the roscoelite structure is fundamental to decipher its site occupancy and to develop new methods for its extraction, but susceptibility to beam damage needs to be considered. An approach combining measurements and modeling of the kind we report here could allow for a better understanding of the 3d metal recovery efficiency in phyllosilicates ores.

Supplementary material

To view supplementary material for this article, please visit https://doi.org/10.1093/micmic/ozac057.

Acknowledgments

We thank Associate Editor Dr. Steven Spurgeon and the three anonymous reviewers for their constructive reviews that helped to improve the clarity of the manuscript. Research supported by the NASA Emerging Worlds (80NSSC19K0509) and Laboratory Analysis of Returned Samples (80NSSC18K1475) Programs. The DFT results are based on High-Performance Computing (HPC) resources supported by the University of Arizona TRIF, UITS, and Research, Innovation, and Impact (RII) and maintained by the UArizona Research Technologies department. We gratefully acknowledge NASA (grants #NNX12AL47G and #NNX15AJ22G) and NSF (grant #1531243) for funding of the instrumentation in the Kuiper Materials Imaging and Characterization Facility at the Lunar and Planetary Laboratory, University of Arizona. Collection and characterization of the roscoelite sample was a part of work also supported by the NSF (grant #2045277). We thank members of the Planetary Materials Research Group at LPL for helpful discussions. P-M. Z. thanks Ms. Laurinne Valentine Blanche for her help with EELS spectrometer investigation.

Financial support

This research was supported by the NASA Emerging Worlds (80NSSC19K0509) and Laboratory Analysis of Returned Samples (80NSSC18K1475) Programs.

Conflict of interest

The authors declare that they have no competing interest.

References

Ballhaus C, Berry RF & Green DH (1990). Oxygen fugacity controls in the earth's upper mantle. *Nature* **348**(6300), 437–440.

Berry AJ, Danyushevsky LV, O'Neill HSC, Newville M & Sutton SR (2008). Oxidation state of iron in komatiitic melt inclusions indicates hot Archaean mantle. *Nature* **455**, 960–963.

Berry AJ, Schofield PF, Kravtsova AN, Miller LA, Stephen NR, Walker AM, Soldatov AV, Ireland TR, Geraki K & Mosselmans JFW (2017). The limitations of hibonite as a single-mineral oxybarometer for early solar system processes. *Chem Geol* **466**, 32–40.

Blaha P, Schwarz K, Madsen G, Kvasnicka D & Luitz J (2011). WIEN2k, 1–223 p. User's guide, Wien2k_11.1 Vol. 1.

Blaha P, Schwarz K, Tran F, Laskowski R, Madsen GKH & Marks LD (2020). WIEN2k: An APW+lo program for calculating the properties of solids. *J Chem Phys* **152**, 074101.

Bourdelle F, Benzerara K, Beyssac O, Cosmidis J, Neuville DR, Brown GE & Paineau E (2013). Quantification of the ferric/ferrous iron ratio in silicates by scanning transmission X-ray microscopy at the Fe $L_{2,3}$ edges. *Contrib Mineral Petrol* **166**, 423–434.

Brigatti MF, Caprilli E, Marchesini M & Poppi L (2003). The crystal structure of roscoelite-1*M*. *Clays Clay Miner* **51**, 301–308.

Brik MG, Ogasawara K, Ikeno H & Tanaka I (2006). Fully relativistic calculations of the $L_{2,3}$-edge XANES spectra for vanadium oxides. *Eur Phys J B* **51**, 345–355.

Canil D (1997). Vanadium partitioning and the oxidation state of Archaean komatiite magmas. *Nature* **389**, 842–845.

Chi M, Ishii HA, Simon SB, Bradley JP, Dai Z, Joswiak D, Browning ND & Matrajt G (2009). The origin of refractory minerals in comet 81P/wild 2. *Geochim Cosmochim Acta* **73**, 7150–7161.

Cressey G, Henderson CMB & van der Laan G (1993). Use of L-edge X-ray absorption spectroscopy to characterize multiple valence states of 3 d transition metals; a new probe for mineralogical and geochemical research. *Phys Chem Miner* **20**, 111–119.

de la Peña F, Prestat E, Fauske VT, Burdet P, Furnival T, P, Nord M, Ostasevicius T, Lähnemann J, MacArthur KE & others (2022). Hyperspy/hyperspy: Release v1.7.3 Zenodo. https://doi.org/10.5281/zenodo.7263263

D'Elia A, Rezvani SJ, Zema N, Zuccaro F, Fanetti M, Belec B, Li BW, Zou CW, Spezzani C, Sacchi M, Marcelli A & Coreno M (2021). Stoichiometry and disorder influence over electronic structure in nanostructured VOx films. *J Nanopart Res* **23**, 33. https://doi.org/10.1007/s11051-020-05130-z

Drexler MS (2022). Vanadium in phyllosilicates. *Master Thesis*. The University of Arizona, AZ.

Egerton RF (2011). *Electron Energy-Loss Spectroscopy in the Electron Microscope*. 3rd ed. New York Heidelberg Dordrecht London: Springer Science & Business Media. Springer.

Egerton RF (2013). Control of radiation damage in the TEM. *Ultramicroscopy* **127**, 100–108.

Egerton RF, Li P & Malac M (2004). Radiation damage in the TEM and SEM. *Micron* **35**, 399–409.

Ek M, Ramasse QM, Arnarson L, Georg Moses P & Helveg S (2017). Visualizing atomic-scale redox dynamics in vanadium oxide-based catalysts. *Nat Commun* **8**, 305.

Fischer DW (1970). Molecular-orbital interpretation of the soft x-ray LII, III emission and absorption spectra from some titanium and vanadium compounds. *J Appl Phys* **41**, 3561–3569.

Fitting Kourkoutis L, Hotta Y, Susaki T, Hwang HY & Muller DA (2006). Nanometer scale electronic reconstruction at the interface between $LaVO_3$ and $LaVO_4$. *Phys Rev Lett* **97**, 256803.

Foster MD (1959). Chemical study of the mineralized clays. In *Geochemistry and Mineralogy of the Colorado Plateau Uranium Ores*, Garrels ESL & Minard R (Eds.), pp. 121–132. U.S. Geological Survey Professional Paper.

Frost BR (1991). Chapter 1.Introduction to oxygen fugacity and its petrologic importance. *Oxide Minerals*, 1–10.

Frost DJ & McCammon CA (2008). The redox state of earth's Mantle. *Annu Rev Earth Planet Sci* **36**, 389–420.

Gallasch T, Stockhoff T, Baither D & Schmitz G (2011). Ion beam sputter deposition of V_2O_5 thin films. *J Power Sources* **196**, 428–435.

Garrels R & Larsen ES (1959). *Geochemistry and Mineralogy of the Colorado Plateau Uranium Ores (Geological Survey Professional Paper 320)*. USGS Numbered Series, 320 p. Washington, DC: United States Government Printing Office.

Garvie LAJ & Buseck PR (1998). Ratios of ferrous to ferric iron from nanometre-sized areas in minerals. *Nature* **396**, 667–670.

Garvie LAJ, Craven AJ & Brydson R (1994). Use of electron-energy loss near-edge fine structure in the study of minerals. *Am Mineral* **79**, 411–425.

Garvie LAJ, Zega TJ, Rez P & Buseck PR (2004). Nanometer-scale measurements of $Fe^{3+}/\Sigma Fe$ by electron energy-loss spectroscopy: A cautionary note. *Am Mineral* **89**, 1610–1616.

Giannini M (2014) The crystal chemistry of hibonite: An indicator for oxygen fugacity during solar nebula condensation? *PhD Thesis*. University of Bayreuth, Bayreuth, Germany.

Hébert C (2007). Practical aspects of running the WIEN2k code for electron spectroscopy. *Micron* **38**, 12–28.

Hébert C, Luitz J & Schattschneider P (2003). Improvement of energy loss near edge structure calculation using Wien2k. In *Micron*, vol. **34**. pp. 219–225.

Holtstam D (1996). Iron in hibonite: A spectroscopic study. *Phys Chem Miner* **23**, 452–460.

Ilett M, S'ari M, Freeman H, Aslam Z, Koniuch N, Afzali M, Cattle J, Hooley R, Roncal-Herrero T, Collins SM & others (2020). Analysis of complex, beam-sensitive materials by transmission electron microscopy and associated techniques. *Philos Trans A Math Phys Eng Sci* **378**, 20190601.

Jacquemot P, Viennet JC, Bernard S, Le Guillou C, Rigaud B, Delbes L, Georgelin T & Jaber M (2019). The degradation of organic compounds impacts the crystallization of clay minerals and vice versa. *Sci Rep* **9**, 20251.

Jayasuriya KD, O'Neill HSC, Berry AJ & Campbell SJ (2004). A Mössbauer study of the oxidation state of Fe in silicate melts. *Am Mineral* **89**, 1597–1609.

Jorissen K (2007). The ab initio calculation of relativistic electron energy loss spectra. *PhD Thesis*. University of Antwerp, Antwerp, Belgium.

Kalavathi S, Amirthapandian S, Chandra S, Sahu PC & Sahu HK (2014). Valence state, hybridization and electronic band structure in the charge ordered AlV_2O_4. *J Phys: Condens Matter* **26**, 015601.

Ketelaar AA (1936). Die Kristallstruktur des Vanadinpentoxyds. Zeitschrift für Kristallographie-Crystalline Materials **95**(1-6), 9–27.

Kurmaev EZ, Ankudinov AL, Rehr JJ, Finkelstein LD, Karimov PF & Moewes A (2005). The L_2:L_3 intensity ratio in soft X-ray emission spectra of 3d-metals. *J Electron Spectros Relat Phenomena* **148**, 1–4.

Lamsal C (2014). Electronic, thermoelectric and optical properties of vanadium oxides : VO2, V2O3 and V2O5. *PhD Thesis*, New Jersey Institute of Technology, NJ.

Leapman RD, Grunes LA & Fejes PL (1982). Study of the L23 edges in the 3d transition metals and their oxides by electron-energy-loss spectroscopy with comparisons to theory. *Phys Rev B* **26**, 614–635.

Le Guillou C, Changela GH, Brearley AJ, Changela HG & Brearley AJ (2015). Widespread oxidized and hydrated amorphous silicates in CR chondrites matrices: Implications for alteration conditions and H2 degassing of asteroids. *Earth Planet Sci Lett* **420**, 162–173.

Levina A, McLeod AI & Lay PA (2014). Vanadium speciation by XANES spectroscopy: A three-dimensional approach. *Chem - A Eur J* **20**, 12056–12060.

Li X, Dyck O, Kalinin SV & Jesse S (2018). Compressed sensing of scanning transmission electron microscopy (STEM) with nonrectangular scans. *Microsc Microanal* **24**, 623–633.

Li J, Gauntt BD, Kulik J & Dickey EC (2009). Stoichiometry of nanocrystalline VOx thin films determined by electron energy loss spectroscopy. *Microsc Microanal* **15**, 1004–1005.

Loehman RE, Rao CNR & Honig JM (1969). Crystallography and defect chemistry of solid solutions of vanadium and titanium oxides. *J Phys Chem* **73**, 1781–1784.

Marcelli A, Coreno M, Stredansky M, Xu W, Zou C, Fan L, Chu W, Wei S, Cossaro A, Ricci A & others (2017). Nanoscale phase separation and lattice complexity in VO2: The metal–insulator transition investigated by xanes via auger electron yield at the vanadium l23-edge and resonant photoemission. *Condens Matter* **2**, 1–11.

Meunier JD (1994). The composition and origin of vanadium-rich clay minerals in Colorado plateau jurassic sandstones. *Clays Clay Miner* **42**(4), 391–401.

Mignaioli E, Capitani G, Nieto F & Mellini M (2009). Accurate and precise lattice parameters by selected-area electron diffraction in the transmission electron microscope. *Am Mineral* **94**, 793–800.

Moretti R & Neuville DR (2021). *Redox Equilibria* pp. 1–17. Hoboken, NJ: Geophysical Monograph Series, American Geophysical Union.

Muller DA, Fitting Kourkoutis L, Murfitt M, Song JH, Hwang HY, Silcox J, Dellby N & Krivanek OL (2008). Atomic-scale chemical imaging of composition and bonding by aberration-corrected microscopy. *Science* **319**, 1073–1076.

Mysen BO, Virgo D & Seifert FA (1984). Redox equilibria of iron in alkaline earth silicate melts: Relationships between melt structure, oxygen fugacity, temperature and properties of iron-bearing silicate liquids. *Am Mineral* **69**, 834–847.

Newnham EE & De Haan YM (1962). Refinement of the a Al_2O_3, Ti_2O_3, V_2O_3 and Cr_2O_3 structures. *Zeitschrift für Kristallographie-Crystalline Materials* **117**(1-6), 235–237.

Nicklas RW, Puchtel IS & Ash RD (2016). High-precision determination of the oxidation state of komatiite lavas using vanadium liquid-mineral partitioning. *Chem Geol* **433**, 36–45.

Nuñez M (2019). Exploring materials band structure space with unsupervised machine learning. *Comput Mater Sci* **158**, 117–123.

Ostrooumov M & Taran Y (2016). Vanadium, V—a new native element mineral from the Colima volcano, State of Colima, Mexico, and implications for fumarole gas composition. *Mineral Mag* **80**, 371–382.

Perdew JP, Burke K & Ernzerhof M (1996). Generalized gradient approximation made simple. *Phys Rev Lett* **77**, 3865–3868.

Petit PE, Farges F, Wilke M & Solé VA (2001). Determination of the iron oxidation state in earth materials using XANES pre-edge information. *J Synchrotron Radiat* **8**, 952–954.

Prytulak J, Nielsen SG, Ionov DA, Halliday AN, Harvey J, Kelley KA, Niu YL, Peate DW, Shimizu K & Sims KWW (2013). The stable vanadium isotope composition of the mantle and mafic lavas. *Earth Planet Sci Lett* **365**, 177–189.

Radwany M (2021). Geometallurgical characterization of sandstone-hosted vanadium ore from the Colorado plateau. *Master Thesis*, The University of Arizona, AZ.

Radwany MR & Barton IF (2022). The process mineralogy of leaching sandstone-hosted uranium-vanadium ores. *Miner Eng* **187**, 107811.

Rakotoniaina JC, Mokrani-Tamellin R, Gavarri JR, Vacquier G, Casalot A & Calvarin G (1993). The thermochromic vanadium dioxide. I. Role of stresses and substitution on switching properties. *J Solid State Chem* **103**, 81–94.

Righter K, Drake MJ & Scott ERD (2006). Compositional relationships between meteorites and terrestrial planets. In *Meteorites and the Early Solar System II*, vol. **943**, pp. 803–828. Tucson, AZ: The University of Arizona Press (UA Press).

Righter K, Sutton SR, Danielson L, Pando K & Newville M (2016). Redox variations in the inner solar system with new constraints from vanadium XANES in spinels. *Am Mineral* **101**, 1928–1942.

Roskosz M, Dauphas N, Hu J, Hu MY, Neuville DR, Brown D, Bi W, Nie NX, Zhao J & Alp EE (2022). Structural, redox and isotopic behaviors of iron in geological silicate glasses: A NRIXS study of Lamb-Mössbauer factors and force constants. *Geochim Cosmochim Acta* **321**, 184–205.

Schreiber HD, Thanyasiri T, Lach JJ & Legere RA (1978). Redox equilibria of Ti, Cr, and Eu in silicate melts: reduction potentials and mutual interactions. *Phys Chem Glasses* **19**, 126–139.

Simon SB, Sutton SR & Grossman L (2007). Valence of titanium and vanadium in pyroxene in refractory inclusion interiors and rims. *Geochim Cosmochim Acta* **71**, 3098–3118.

Sparrow TG, Williams BG, Rao CNR & Thomas JM (1984). L3/L2 white-line intensity ratios in the electron energy-loss spectra of 3d transition-metal oxides. *Chem Phys Lett* **108**, 547–550.

Stevens AJ (2018). Compressive sensing in transmission electron microscopy. *PhD Thesis*. Duke University, Durham, NC, p. 178.

Stoyanov E, Langenhorst F & Steinle-Neumann G (2007). The effect of valence state and site geometry on Ti $L_{3,2}$ and O K electron energy-loss spectra of Ti_xO_y phases. *Am Mineral* **92**, 577–586.

Su DS & Schlögl R (2002). Thermal decomposition of divanadium pentoxide V_2O_5: Towards a nanocrystalline V_2O_3 phase. *Catal Letters* **83**(3), 115–119.

Taillon JA (2018). Compressive sensing reconstruction for EDS analysis. *Microsc Microanal* **24**, 486–487.

Tan H, Turner S, Yücelen E, Verbeeck J & Van Tendeloo G (2011). 2D Atomic mapping of oxidation states in transition metal oxides by scanning transmission electron microscopy and electron energy-loss spectroscopy. *Phys Rev Lett* **107**, 107602.

Tan H, Verbeeck J, Abakumov A & Van Tendeloo G (2012). Oxidation state and chemical shift investigation in transition metal oxides by EELS. *Ultramicroscopy* **116**, 24–33.

Tian M, Wang XD & Zhang T (2016). Hexaaluminates: A review of the structure, synthesis and catalytic performance. *Catal Sci Technol* **6**(7), 1984–2004. https://doi.org/10.1039/C5CY02077H

Van Aken PA & Liebscher B (2002). Quantification of ferrous/ferric ratios in minerals: New evaluation schemes of Fe L_{23} electron energy-loss near-edge spectra. *Phys Chem Miner* **29**, 188–200.

Van Aken PA, Liebscher B & Styrsa VJ (1998). Quantitative determination of iron oxidation states in minerals using Fe $L_{2,3}$-edge electron energy-loss near-edge structure spectroscopy. *Phys Chem Miner* **25**, 323–327.

Virdi KS, Kauffmann Y, Ziegler C, Ganter P, Lotsch BV, Kaplan WD, Blaha P & Scheu C (2013). Electronic structure of KCa2Nb3O10 as envisaged by density functional theory and valence electron energy loss spectroscopy. *Phys Rev B* **87**, 115108.

Wanty R & Goldhaber M (1985). A method for the determination of vanadium and iron oxidation states in naturally occurring oxides and silicates. *Talanta* **32**, 395–398.

Xu H & Wang Y (1999). Electron energy-loss spectroscopy (EELS) study of oxidation states of ce and U in pyrochlore and uraninite —natural analogues for Pu- and U-bearing waste forms. *J Nucl Mater* **265**, 117–123.

Zanetta P-M, Manga VR, Chang Y, Ramprasad T, Beckett JR, Zega TJ & Sciences P (2022). Atomic-scale characterization of the oxidation state of Ti in meteoritic hibonite: Implications for early solar system thermodynamics. *Am Mineral*. https://doi.org/10.2138/am-2022-8311

Zega TJ, Garvie LAJ & Buseck PR (2003). Nanometer-scale measurements of iron oxidation states of cronstedtite from primitive meteorites. *Am Mineral* **88**, 1169–1172.

Zega TJ, Haenecour P & Floss C (2020). An in situ investigation on the origins and processing of circumstellar oxide and silicate grains in carbonaceous chondrites. *Meteorit Planet Sci* **55**, 1207–1227.

Zega TJ, Nittler LR, Busemann H, Hoppe P & Stroud RM (2007). Coordinated isotopic and mineralogic analyses of planetary materials enabled by in situ lift-out with a focused ion beam scanning electron microscope. *Meteorit Planet Sci* **42**, 1373–1386.

Zheng Q, Zhang Y, Liu T, Huang J & Xue N (2019). Vanadium extraction from black shale: Enhanced leaching due to fluoride addition. *Hydrometallurgy* **187**, 141–148.

Zheng Q, Zhang Y & Xue N (2022). Enhancing effect of vanadium releasing efficiently from lattice in black shale by thermal activation. *Colloids Surf A: Physicochem Eng Aspects* **651**, 129773.

Zhou Y & Ramanathan S (2015). Mott memory and neuromorphic devices. *Proc IEEE* **103**, 1289–1310.